Computational Materials Science 46 (2009) 479–490

Contents lists available at ScienceDirect

Computational Materials Science

journal homepage: www.elsevier.com/locate/commatsci

Comparative study of two phase-field models for grain growth

Nele Moelans [a,b,*], Frank Wendler [c], Britta Nestler [c]

[a] Dept. Metallurgy and Materials Engineering, Katholieke Universiteit Leuven, Kasteelpark Arenberg 44 – Bus 2450, B-3001 Leuven, Belgium
[b] Condensed Matter and Materials Division, Lawrence Livermore National Laboratory, 7000 East Avenue, Livermore, CA 94551, USA
[c] Institute of Computational Engineering, Karlsruhe University of Applied Sciences, Moltkestrasse 30, D-76133 Karlsruhe, Germany

ARTICLE INFO

Article history:
Received 24 February 2009
Received in revised form 25 March 2009
Accepted 27 March 2009
Available online 28 April 2009

PACS:
68.35.bd
81.07.Bc
05.10.−a
61.72.−y
87.16.−b
89.75.Da

Keywords:
Grain growth
Phase-field modeling
Grain boundary migration
Numerical simulation
Microstructure
Model validation

ABSTRACT

There exist different phase-field models for the simulation of grain growth in polycrystalline structures. In this paper, the model formulation, application and simulation results are compared for two of these approaches. First, we derive relations between the parameters in both models that represent the same set of grain boundary energies and mobilities. Then, simulation results obtained with both models, using equivalent model parameters, are compared for grain structures in 2D and 3D. The evolution of the individual grains, grain boundaries and triple junction angles is followed in detail. Moreover, the simulation results obtained with both approaches are compared using analytical theories and previous simulation results as benchmarks. We find that both models give essentially the same results, except for differences in the structure near small shrinking grains which are most often locally and temporary for large grain structures.

1. Introduction

Phase-field modeling is widely used to study the microstructural evolution in alloys during phase transformations and grain growth, see e.g. [1–4]. Common to all phase-field models of the Allen–Cahn or Ginzburg–Landau type is that the microstructure is described with nonconserved field variables, which represent for example, the local structure and orientation. Interfaces are treated as diffuse transitions in the value of one or more of these fields over a narrow region. Most often, the evolution equations for the fields are derived from a phenomenological free energy following Onsager's principles. The equations contain parameters that are related to physical properties of the system, such as surface energy and mobility. There are however several possibilities to choose a set of phase fields, the model parameters and the form of the free energy functional, from which the evolution equations are derived. For many microstructural processes, different phase-field models have been developed, all producing simulation results that are often in good agreement with analytical models or experimental data. The existence of multiple model formulations and different definitions of the model parameters is however confusing when exchanging simulation results or if one wants to integrate the phase-field technique with other modeling techniques, for instance in a multi-scale approach.

In this paper, two different phase-field approaches that have been applied frequently to grain growth are compared, namely that originating from the work of Chen and Yang [5] and Fan and Chen [6], which will be referred as the *continuum-field (CF)* model, and that originating from Steinbach et al. [7] and Garcke et al. [8], referred as the *multi-phase-field (MPF)* model. In both models, a large set of non-conserved phase fields (or order parameter fields) is used to represent the different grain orientations. A major distinction is in the interpretation of the phase fields. In continuum-field models, the field variables are treated as being independent. At the diffuse grain boundaries, the variables change monotonously between values without any constraint. In multi-phase-field models, in contrast, the phase fields are interpreted as volume

* Corresponding author. Address: Dept. Metallurgy and Materials Engineering, Katholieke Universiteit Leuven, Kasteelpark Arenberg 44 – Bus 2450, B-3001 Leuven, Belgium.
E-mail address: Nele.Moelans@mtm.kuleuven.be (N. Moelans).

0927-0256/$ - see front matter © 2009 Elsevier B.V. All rights reserved.
doi:10.1016/j.commatsci.2009.03.037

fractions which therefore are subject to the constraint that the sum of the phase fields must be equal to one at each position in the system. Furthermore, the thermodynamic free energy in the continuum-field model has multiple degenerate minima, one for each grain orientation. The free energy of the multi-phase-field model has a single minimum for all phase fields equal to zero. It is the constraint on the sum of the phase fields that forces one of them to equal 1 within the grains. From a mathematical point of view, the evolution equations obtained in the two approaches, have different solutions. The diffuse transitions at interfaces have for example a different shape [8,9]. Large-scale simulations [6,10–12] have shown that both models give similar grain growth behavior with statistics close to those expected from mean field theories for normal grain growth, if a sufficiently large number of grains is considered and grain coalescence is avoided [11,12]. The purpose of this paper is to compare these two phase-field approaches in more detail. The multi-phase-field and continuum-field model as formulated in respectively [13] and [14,9] are considered in particular. First, we compare the model formulation and derive relationships between the parameters in both models in Section 2. Numerical aspects and parameter choices are shortly discussed in Section 3. In Section 4, simulation results for both models using equivalent parameter values are compared with analytical models for simple grain geometries and in Section 5, the growth behavior of individual grains and small grain assemblies embedded in larger grain structures is studied. Statistical quantities typically used to characterize grain growth behavior are also determined and compared with classical theories to analyse the impact on the overall statistical properties of small deviations on a local scale. Besides these two approaches, there exist other phase-field models for multi-grain structures [15,16]. They are not considered in this study.

2. Model comparison

2.1. Model formulation

We refer to [8,17,13] and [6,18,14,9] for more details on respectively the multi-phase-field and continuum-field models.

In the multi-phase-field model, the Helmholtz free energy functional for a single-phase multi-grain structure is constructed as

$$F = \int_V \varepsilon a(\boldsymbol{\phi}, \nabla\boldsymbol{\phi}) + \frac{1}{\varepsilon} w(\boldsymbol{\phi}) \mathrm{d}V, \tag{1}$$

with $a(\boldsymbol{\phi}, \nabla\boldsymbol{\phi})$ the gradient free energy density, $w(\boldsymbol{\phi})$ the potential and $\boldsymbol{\phi}$ the N-component phase field vector $(\phi_1, \ldots, \phi_\alpha, \ldots, \phi_N)$ representing N different grain orientations with each component. Following the derivation of the model in [17], it must be postulated that the state variables ϕ_α all sum up to unity in each point of space, $\sum_\alpha \phi_\alpha = 1$ as well as $0 \leqslant \phi_\alpha \leqslant 1\,(\alpha \in \{1 \cdots N\})$, i.e. $\boldsymbol{\phi}$ lies on a Gibbs simplex. Therefore, each component ϕ_α can be regarded as the volume fraction of grain α, which is important for ensuring correct energy contributions in each point of the interface. The energy density contribution $w(\boldsymbol{\phi})$ in (1) is chosen to be of a multi-obstacle type with N sharp defined minima at the bulk phases states $(\phi_\alpha = 1, \phi_{\beta(\beta\neq\alpha)} = 0)$. In the allowed range for $\boldsymbol{\phi}$, $w(\boldsymbol{\phi})$ calculates as

$$w(\boldsymbol{\phi}) = \frac{16}{\pi^2} \sum_{\alpha<\beta} \gamma_{\alpha\beta} \phi_\alpha \phi_\beta + \sum_{\alpha<\beta<\delta} \gamma_{\alpha\beta\delta} \phi_\alpha \phi_\beta \phi_\delta, \tag{2}$$

and tends to $+\infty$ when outside the Gibbs simplex. The double summation in (2) spans all possible α/β combinations with $\gamma_{\alpha\beta}$ the free energy of the respective α/β-boundary. The second addend in (2) represents a triple summation of all existing higher order terms $\sim \phi_\alpha\phi_\beta\phi_\delta$. This potential modification is necessary to prevent the spontaneous generation of small contributions of third phases in a two-phase boundary ('ghost phases'). For this purpose $\gamma_{\alpha\beta\delta}$ should assume a value of about 10 times the greatest surface energy $\gamma_{\alpha\beta}$ in the system. The gradient free energy density in functional (1)

$$a(\boldsymbol{\phi}, \nabla\boldsymbol{\phi}) = \sum_{\alpha<\beta} \gamma_{\alpha\beta} |\vec{q}_{\alpha\beta}|^2, \tag{3}$$

is formulated as a function of generalized gradient vectors $\vec{q}_{\alpha\beta} = \phi_\alpha \nabla\phi_\beta - \phi_\beta \nabla\phi_\alpha$. This allows to assign different grain boundary energies depending on the angle of misorientation between neighboring grains. Additionally, a dependancy on the inclination of an α/β-boundary can be established by letting $\gamma_{\alpha\beta}$ be a function of $\vec{q}_{\alpha\beta}$. The evolution of the grain structure is given by a set of N kinetic equations for the phase fields ϕ_α which are derived by taking the variational derivative of the free energy

$$\tau\epsilon \frac{\partial\phi_\alpha}{\partial t} = -\frac{\delta F}{\delta\phi_\alpha} - \lambda, \tag{4}$$

$$= \varepsilon(\nabla \cdot a_{,\nabla\phi_\alpha}(\boldsymbol{\phi}, \nabla\boldsymbol{\phi}) - a_{,\phi_\alpha}(\boldsymbol{\phi}, \nabla\boldsymbol{\phi})) - \frac{1}{\varepsilon} w_{,\phi_\alpha}(\boldsymbol{\phi}) - \lambda, \tag{5}$$

where the Lagrange multiplier λ

$$\lambda = \frac{1}{N} \sum_\alpha \left[\varepsilon(\nabla \cdot a_{,\nabla\phi_\alpha}(\boldsymbol{\phi}, \nabla\boldsymbol{\phi}) - a_{,\phi_\alpha}(\boldsymbol{\phi}, \nabla\boldsymbol{\phi})) - \frac{1}{\varepsilon} w_{,\phi_\alpha}(\boldsymbol{\phi}) \right], \tag{6}$$

accounts for the restriction $\sum_\alpha \phi_\alpha = 1$. The parameters ϵ, $\gamma_{\alpha\beta}$ and τ are related to physical grain boundary properties (see Section 2.2).

In the continuum-field model for grain growth [14,9], the free energy functional has the form

$$F = \int_V m f_0(\eta_\alpha, \eta_\beta, \ldots, \eta_N) + \frac{\kappa}{2} \sum_\alpha (\nabla\eta_\alpha)^2 \mathrm{d}V, \tag{7}$$

with $f_0(\eta_\alpha, \eta_\beta, \ldots, \eta_N)$ a fourth order polynomial of the phase fields $(\eta_\alpha, \eta_\beta, \ldots, \eta_N)$

$$f_0 = \sum_\alpha \left(\frac{\eta_\alpha^4}{4} - \frac{\eta_\alpha^2}{2} \right) + \sum_{\alpha<\beta} \gamma'_{\alpha\beta} \eta_\alpha^2 \eta_\beta^2, \tag{8}$$

with $2N$ minima of equal depth ($f_{0,\min} = -0.25$) at $(\ldots, 0, \pm1, 0, \ldots)$ representing N grain orientations. The minima at $(\ldots, 0, +1, 0, \ldots)$ and $(\ldots, 0, -1, 0, \ldots)$ correspond to the same grain orientation. In this study, we only consider the minimum at $(\ldots, 0, +1, 0, \ldots)$. The temporal evolution of the phase fields follows an equation of the form

$$\frac{\partial\eta_\alpha}{\partial t} = -L\left(m \frac{\partial f_0}{\partial\eta_\alpha} - \kappa\nabla^2\eta_\alpha \right), \tag{9}$$

for all η_α. In order to distinguish between different grain boundary energies depending on the misorientation between neighboring grains, the energy gradient coefficient κ is formulated as a function of the phase fields

$$\kappa = \frac{\sum_{\alpha<\beta} \kappa_{\alpha\beta} \eta_\alpha^2 \eta_\beta^2}{\sum_{\alpha<\beta} \eta_\alpha^2 \eta_\beta^2}. \tag{10}$$

This formulation results in constant values for κ at the diffuse interfaces between different grains. The parameters $\kappa_{\alpha\beta}$ and $\gamma'_{\alpha\beta}$ are related to the properties of the interface between grains α and β. In Section 2.2, it is shown how the parameters m, $\kappa_{\alpha\beta}$, $\gamma'_{\alpha\beta}$ and L relate to physical grain boundary properties.

2.2. Model parameters

For the MPF model considered in this study [13] the parameters $\gamma_{\alpha\beta}$ equal the specific free energies $\sigma_{\alpha\beta}$ of the grain boundaries between two grains with orientations α and β, and the parameter ε is a measure for the width of the diffuse interfaces, which will be

considered in greater detail in Section 2.3. Furthermore, all grain boundaries have the same mobility, namely $\mu = 1/\tau$, with τ the kinetic factor in the MPF Eq. (5).

For the CF model the relation between the grain boundary energy $\sigma_{\alpha\beta}$ and the parameters in the free energy functional can be expressed as [9]

$$\sigma_{\alpha\beta} = g(\gamma'_{\alpha\beta})\sqrt{m\kappa_{\alpha\beta}}. \tag{11}$$

with $g(\gamma'_{\alpha\beta})$ a function that must be obtained by numerical evaluation of the integral

$$\sigma_{\alpha\beta} = \sqrt{m\kappa_{\alpha\beta}}\int_0^1 \sqrt{2(f_0 - f_{0,\min})}\sqrt{1+\left(\frac{\mathrm{d}\eta_\beta}{\mathrm{d}\eta_\alpha}\right)^2}\,\mathrm{d}\eta_\alpha, \tag{12}$$

for different values of $\gamma'_{\alpha\beta}$. Furthermore, the product $L\kappa_{\alpha\beta}$ in the CF model equals the reduced grain boundary mobility $\mu^* = \mu\sigma_{\alpha\beta}$ and, for a fixed value of $\gamma'_{\alpha\beta}$, the diffuse interface width is proportional to $\sqrt{\kappa_{\alpha\beta}/m}$.

For two-grain structures, the MPF model reduces to a classical phase-field model with one evolution equation for a single phase-field variable taking the value 1 within one grain and 0 in the other, remaining the same relations between model parameters and physical quantities. This is not the case for the CF model.

2.3. Equivalent parameter combinations

From a mathematical point of view, the interpretation of the field variables is different for both approaches. There exists, therefore, no straightforward relation between the phase fields in both models that transforms one model formulation into the other. However, it is possible to derive relationships between their model parameters for given system properties. In the case of grain growth, for each interface α/β, three parameters in the MPF model ($\gamma_{\alpha\beta}, \varepsilon$ and τ) must be related to four parameters in the CF model ($m, \kappa_{\alpha\beta}$, $\gamma'_{\alpha\beta}$ and L) so that the grain boundary properties and grain growth kinetics obtained in the simulations are the same for both models.

As a first requirement the grain boundary energies $\sigma_{\alpha\beta}$ must be equal for both model formulations, giving

$$\gamma_{\alpha\beta} = g(\gamma'_{\alpha\beta})\sqrt{\kappa_{\alpha\beta}m}. \tag{13}$$

Next, in order to have the same grain growth kinetics, the reduced grain boundary mobility $\mu^* = \mu\sigma_{\alpha\beta}$ should be equal, resulting in

$$\frac{1}{\tau}\gamma_{\alpha\beta} = L\kappa_{\alpha\beta}, \tag{14}$$

Although it will be illustrated in Section 4.2 that the profiles of the phase fields at interfaces are different for both models, (and it is thus impossible to give the diffuse interfaces exactly the same width in both models) equivalent sets of model parameters should result in a 'comparable' interfacial width. Therefore, we will require that the maximum gradient of the phase fields in the direction perpendicular to the interface is equal in the MPF and CF simulations. Since the phase-field profiles have their maximum gradient at the middle of an interface where the profiles of two phase fields cross, we expect that this equality results in comparable numerical stability and accuracy for both models. In this way, 'equal interface width' means equal numerical accuracy and stability requirements.

If it is assumed that at an interface only two phase fields differ from 0, which is approximately the case, the restriction $\sum_\alpha \phi_\alpha = 1$ in the MPF model gives $\phi_\alpha + \phi_\beta = 1$ and $\nabla\phi_\alpha = -\nabla\phi_\beta$. The total free energy density in the functional in Eq. (1) accordingly reduces to

$$f = \varepsilon\gamma_{\alpha\beta}(\nabla\phi_\alpha)^2 + \frac{1}{\varepsilon}w(\phi_\alpha, 1-\phi_\alpha). \tag{15}$$

From this formula, it can be calculated using an integrated form of the Euler–Lagrange equation that

$$\left|\frac{\mathrm{d}\phi_\alpha}{\mathrm{d}x}\right| = \pm\sqrt{\frac{(\phi_\alpha, 1-\phi_\alpha)}{\varepsilon^2\gamma_{\alpha\beta}}} \tag{16}$$

with x measured along the direction perpendicular to the interface. Due to the restriction $\phi_\alpha + \phi_\beta = 1$, the phase fields always cross at $\phi_\alpha = \phi_\beta = 0.5$ and accordingly $w = (4/\pi^2)\gamma_{\alpha\beta}$ at the middle of the interface. Therefore

$$\left(\left|\frac{\mathrm{d}\phi_\alpha}{\mathrm{d}\,x}\right|\right)_{\max} = \left(\left|\frac{\mathrm{d}\phi_\beta}{\mathrm{d}x}\right|\right)_{\max} = \sqrt{\frac{4}{\pi^2\varepsilon^2}}. \tag{17}$$

For the CF model, the free energy density at interfaces between two grains equals

$$f = \frac{\kappa_{\alpha\beta}}{2}\left((\nabla\eta_\alpha)^2 + (\nabla\eta_\beta)^2\right) + mf_0(\eta_\alpha, \eta_\beta), \tag{18}$$

as there is no restriction that relates the evolution of the two phase fields. The gradients of the phase fields are given by

$$\frac{\mathrm{d}\eta_\alpha}{\mathrm{d}x} = \pm\sqrt{\frac{2m(f_0 - f_{0,\min})}{\kappa_{\alpha\beta}\left(1+\left(\frac{\mathrm{d}\eta_\beta}{\mathrm{d}\eta_\alpha}\right)^2\right)}} \quad \text{and} \quad \frac{\mathrm{d}\eta_\beta}{\mathrm{d}x} = \mp\sqrt{\frac{2m(f_0 - f_{0,\min})}{\kappa_{\alpha\beta}\left(1+\left(\frac{\mathrm{d}\eta_\alpha}{\mathrm{d}\eta_\beta}\right)^2\right)}}. \tag{19}$$

From the symmetry of the free energy density (18) with respect to η_α and η_β it follows that $\mathrm{d}\eta_\alpha/\mathrm{d}\eta_\beta = \mathrm{d}\eta_\beta/\mathrm{d}\eta_\alpha = -1$ at the middle of the interface where $\eta_\alpha = \eta_\beta = \eta_{\mathrm{int}}$. Therefore

$$\begin{aligned}\left(\left|\frac{\mathrm{d}\eta_\alpha}{\mathrm{d}x}\right|\right)_{\max} &= \left(\left|\frac{\mathrm{d}\eta_\beta}{\mathrm{d}x}\right|\right)_{\max} = \sqrt{\frac{m(f_{0,\mathrm{int}} - f_{0,\min})}{\kappa_{\alpha\beta}}} \\ &= \frac{3}{4}a(\gamma'_{\alpha\beta})g(\gamma'_{\alpha\beta})\sqrt{\frac{m}{\kappa_{\alpha\beta}}},\end{aligned} \tag{20}$$

with $f_{0,\mathrm{int}} = f_0(\eta_{\mathrm{int}})$ the value of f_0 at the middle of the interface, which depends on the parameter $\gamma'_{\alpha\beta}$. The factor $a(\gamma'_{\alpha\beta})$ can be calculated numerically [9] as a function of $\gamma'_{\alpha\beta}$. It is close to 1 for practical values of $\gamma'_{\alpha\beta}$.

From (17) and (20), it follows that in order to have equal maximum gradients

$$\frac{1}{\varepsilon^2} = \frac{9\pi^2}{64}\frac{m\left(a(\gamma'_{\alpha\beta})\right)^2\left(g(\gamma'_{\alpha\beta})\right)^2}{\kappa_{\alpha\beta}} = \frac{ma'^2\left(g(\gamma'_{\alpha\beta})\right)^2}{\kappa_{\alpha\beta}}, \tag{21}$$

with $a'^2 = (9\pi^2/64)(a(\gamma'_{\alpha\beta}))^2$.

Then, equalities (13), (14) and (21) allow to derive relationships between the parameters in the two phase-field models. In Table 1, formulas are listed that convert the parameters for one model into an equivalent set of parameters for the other. For the same set of parameter values in the MPF model, different combinations of m and $\gamma'_{\alpha\beta}$ in the CF model are possible, but $\xi_{\alpha\beta} = m(g(\gamma'_{\alpha\beta}))^2$ is fixed. The model parameters $\gamma_{\alpha\beta\delta}$ of the potential energy density $w(\boldsymbol{\phi})$

Table 1
Conversion formulas for the parameters in the multi-phase-field (MPF) and continuum-field (CF) model ($\xi_{\alpha\beta} = m(g(\gamma'_{\alpha\beta}))^2$, $a' = (3\pi/4)a(\gamma'_{\alpha\beta})$).

Multi-phase-field → continuum-field	Continuum-field → multi-phase-field
$\kappa_{\alpha\beta} = a'\varepsilon\gamma_{\alpha\beta}$	$\varepsilon = \sqrt{\frac{\kappa_{\alpha\beta}}{\xi_{\alpha\beta}}}\frac{1}{a'}$
$L = \frac{1}{a'\varepsilon\tau}$	$\frac{1}{\tau} = L\sqrt{\frac{\kappa_{\alpha\beta}}{\xi_{\alpha\beta}}}$
$\xi_{\alpha\beta} = \frac{\gamma_{\alpha\beta}}{a'\varepsilon}$	$\gamma_{\alpha\beta} = \sqrt{\kappa_{\alpha\beta}\xi_{\alpha\beta}}$

calibrate the grain boundary energies $\gamma_{\alpha\beta}$ of the MPF model by avoiding the occurrence of ghost phases. They have no direct physical interpretation and are therefore not related to any model parameter in the CF model.

The advantage of the MPF model is that most parameters are directly related to physical quantities, whereas it requires the numerical calculation of an integral to relate the model parameters in the CF model to physical quantities. In the MPF model, on the other hand, third-order interaction coefficients in the free energy potential $\sim \gamma_{\alpha\beta\delta}\phi_\alpha\phi_\beta\phi_\delta$ are required to prevent unwanted phase fields from contributing at interfaces. Depending on the system properties, it can be cumbersome to find appropriate values for these coefficients, as they are not related to a physical quantity.

3. Numerical aspects

In this study, a finite difference discretization with explicit time stepping was used for the numerical solution of the equations for both models. A five point central scheme was used to calculate the Laplacians in the CF Eq. (9). The term $\nabla\cdot(\phi_\alpha\nabla\phi_\beta)$ in the MPF equations (5) was calculated as follows. First, the term $\nabla\phi_\beta$ is calculated using right-sided finite differences and ϕ_α is evaluated in between the grid points on the 'right' side of each grid point. Then, the divergence is calculated using left-sided finite differences. Application of the latter scheme to the Laplacians in the CF equations results in the same finite difference equations as obtained with the central finite difference scheme. In both cases, an equal grid resolution is assumed for the computations in all spatial directions, i.e. $\Delta x = \Delta y = \Delta z$.

For the MPF simulations, grain area A (2D simulations) and volume V (3D simulations) were determined by summing $\phi_\alpha(\Delta x)^2$ or $\phi_\alpha(\Delta x)^3$ over all grid points in the system, with ϕ_α the local fraction of a grain α and Δx the grid spacing. For the CF model, scaled quantities η^*_α

$$\eta^*_\alpha = \frac{\eta^2_\alpha}{\sum_{\beta=1}^{N}\eta^2_\beta}, \tag{22}$$

representing the fraction of a grain α, were defined. Grain area or volume can then be calculated as described above for the MPF simulations, namely by summing $\eta^*_\alpha(\Delta x)^2$ or $\eta^*_\alpha(\Delta x)^3$ over all grid points. The total grain boundary energy in the system is calculated as

$$E_{\mathrm{gb}} = \sum_{\text{grid points}}\left(\varepsilon a(\boldsymbol{\phi},\nabla\boldsymbol{\phi}) + \frac{1}{\varepsilon}w(\boldsymbol{\phi})\right)(\Delta x)^2, \tag{23}$$

for the MPF model and

$$E_{\mathrm{gb}} = \sum_{\text{grid points}}\left(m(f_0 - f_{0,\min}) + \frac{\kappa}{2}\sum\nolimits_\alpha(\nabla\eta_\alpha)^2\right)(\Delta x)^2, \tag{24}$$

for the CF model, respectively. The average grain size of multiple grain structures was computed as $\overline{A} = A_{total}/N$ with A_{total} the area of the simulation box and N the number of grains. The radius R of a grain was calculated from the grain area as $R = \sqrt{A/\pi}$ or from the grain volume as $R = (3\pi V/4)^{1/3}$.

In this paper, spacial dimensions (Δx, ε) will be expressed in 10^{-6}m, time (t, Δt) in s, specific grain boundary energy ($\sigma_{\alpha\beta}$) in J/m^2 and mobility (μ) in 10^{-6}m^2 s/kg. The parameter values do not refer to a particular material, however they are within the range of values typical for metals. The values for Δx, ε are chosen so that a reasonable accuracy is obtained, while keeping grain growth simulations for multi-grain structures computationally feasible. The time step Δt was taken as large as possible considering the stability condition of the explicit finite difference scheme for a given Δx.

4. Two- and three-grain structures

In this section, simulation results obtained with both models for two- and three-grain structures in 2D, are compared. The geometry is chosen so that analytical relations are available as a reference for the comparison. The profiles of the diffuse transitions in the value of the phase fields at interfaces are also compared.

4.1. Shrinking circular grain

First, the shrinkage of a circular grain with orientation α within a matrix with orientation β is considered. Since for curvature driven motion, the velocity $v_{\alpha\beta}$ of the circular boundary between both grains is given by

$$v_{\alpha\beta} = -\frac{\mathrm{d}R_\alpha(t)}{\mathrm{d}t} = \mu\frac{1}{R_\alpha}\sigma_{\alpha\beta}, \tag{25}$$

with $R_\alpha(t)$ the radius of grain α at time t, it follows that, with A_α the area of grain α,

$$\frac{\mathrm{d}A_\alpha}{\mathrm{d}t} = -2\pi\mu\sigma_{\alpha\beta}. \tag{26}$$

The temporal evolution of the area of grain α in the simulations must thus approach the linear relation

$$A_\alpha(t) = A_{\alpha,0} - 2\pi\mu\sigma_{\alpha\beta}t, \tag{27}$$

with $A_{\alpha,0}$ the area of the grain for $t = 0$. Moreover, the total amount of grain boundary energy in the system, calculated as $E_{\mathrm{gb}} = 2\pi R_\alpha\sigma_{\alpha\beta}$, as a function of time should follow the relation

$$E_{\mathrm{gb}}(t) = 2\sqrt{\pi}\sigma_{\alpha\beta}\sqrt{A_{\alpha,0} - 2\pi\mu\sigma_{\alpha\beta}t}, \tag{28}$$

which is equivalent with

$$E^2_{\mathrm{gb}}(t) = E^2_{\mathrm{gb},0} - 8\pi^2\mu\sigma^3_{\alpha\beta}t. \tag{29}$$

In Fig. 1, the temporal evolution of the grain area and total grain boundary energy obtained with both models using equivalent sets of parameter values, are compared with the analytical relations (27) and (29). In Table 2, the relative errors on the rate of shrinkage of the circular grain in the simulated systems are given for different grid spacings Δx and interface widths ε. Only simulation data for $R_\alpha \gg \varepsilon$ were considered when measuring the shrinkage rate. For all three measures, the data lead to the following conclusions. For both models, the accuracy improves with increasing $\varepsilon/\Delta x$-ratio, as a higher $\varepsilon/\Delta x$-ratio gives more grid points to resolve the phase-field profiles at the interface. The accuracy obtained for $\sigma_{\alpha\beta} = 0.2$ and $\sigma_{\alpha\beta} = 0.25$ are nearly the same. Differences in accuracy between both models for fixed simulation parameters are very small in comparison with the effects of changing grid spacing or interfacial width. For both models, the accuracy of the simulation results could be improved further by decreasing the grid spacing; however such small grid spacings are usually not feasible for grain growth simulations for large grain structures.

4.2. Three-grain structure with triple junction

To compare the grain boundary configurations at triple junctions, simulations were performed using a lamellar geometry as illustrated in Fig. 2a with $\sigma_{\alpha\gamma} = \sigma_{\beta\gamma}$, so that the velocity of the grain boundaries α/γ and β/γ and the angles at the triple junction are constant during steady-state motion.

The equilibrium triple junction angle θ, as defined in Fig. 2b, can be calculated using Young's law with $\sigma_{\alpha\gamma} = \sigma_{\beta\gamma}$, giving

$$\theta = 2\arccos\left(\frac{\sigma_{\alpha\beta}}{2\sigma_{\alpha\gamma}}\right). \tag{30}$$

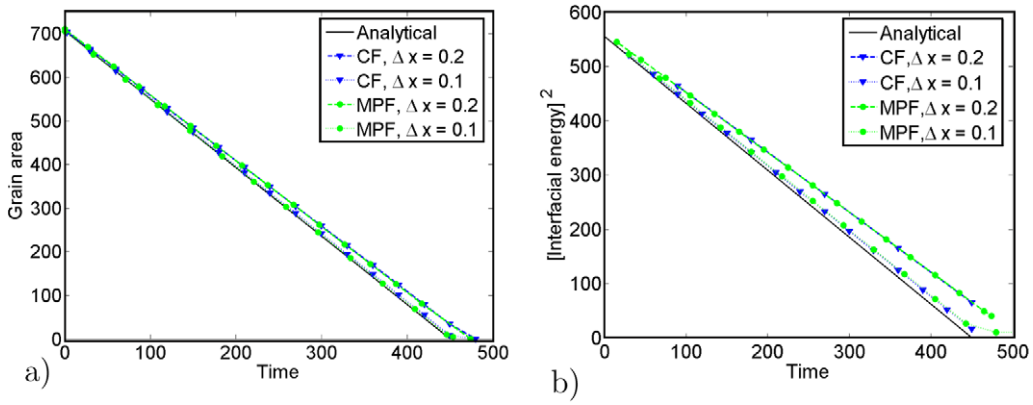

Fig. 1. Evolution of (a) the area and (b) the total grain boundary energy as a function of time for the shrinking circular grain. Simulation results for the multi-phase-field (MPF) and continuum-field (CF) model are compared with the analytical relation for two different grid spacings $\Delta x = 0.1$ and $\Delta x = 0.2$. System parameters: $\sigma_{\alpha\beta} = 0.25$, $\mu = 1$, $\epsilon = 0.5$, $\Delta t = 0.0075$ for $\Delta x = 0.1$ and $\Delta t = 0.03$ for $\Delta x = 0.2$, $R_0 = 15$, $\ell_1 = \ell_2 = 40$.

Furthermore, the Gibbs–Thomson law gives that the velocity of the grain boundaries α/γ and β/γ equals

$$v_{\alpha\gamma} = v_{\beta\gamma} = -\mu\sigma_{\alpha\gamma}\frac{1}{R} = -\mu\frac{\sigma_{\alpha\beta}}{2x_1}. \tag{31}$$

The shrinkage of the area of grain α can accordingly be calculated as

$$\frac{dA_\alpha}{dt} = 2x_1 v_{\alpha\gamma} = -\mu\sigma_{\alpha\beta} \quad \text{and} \quad A_\alpha(t) = A_{\alpha,0} - \mu\sigma_{\alpha\beta}t. \tag{32}$$

Assuming that the grain boundaries α/γ and β/γ maintain constant curvature during grain boundary movement and that the triple junction angles adapt instantaneously to grain boundary movement, the triple junction angle θ was derived from the curvature of the grain boundaries in the simulations as follows. First a circle was fitted through the contour $\phi_\alpha = 0.5$ or $\eta^*_\alpha = 0.5$. The angle θ was then obtained from

Table 2
Shrinkage rate dA_α/dt for the shrinking circular grain for different grid spacings Δx and diffuse interface widths ε. The relative errors are indicated in percentage. System parameters: $\sigma_{\alpha\beta} = 0.25$ (except for $*$ where $\sigma_{\alpha\beta} = 0.2$), $\mu = 1$, $\Delta t = 0.0075$ for $\Delta x = 0.1$ and $\Delta t = 0.03$ for $\Delta x = 0.2$, $R_0 = 15$ and $\ell_1 = \ell_2 = 40$.

ε	Δx	dA_α/dt		
		Anal.	MPF	CF
0.5	0.2	1.57	1.51 (4.1%)	1.52 (3.2%)
1	0.2	1.57	1.56 (0.6%)	1.56 (0.6%)
0.5	0.1	1.57	1.56 (0.8%)	1.56 (0.7%)
1	0.1	1.57	1.57 (<0.1%)	1.57 (<0.1%)
1*	0.1	1.26	1.26 (<0.1%)	1.26 (<0.1%)

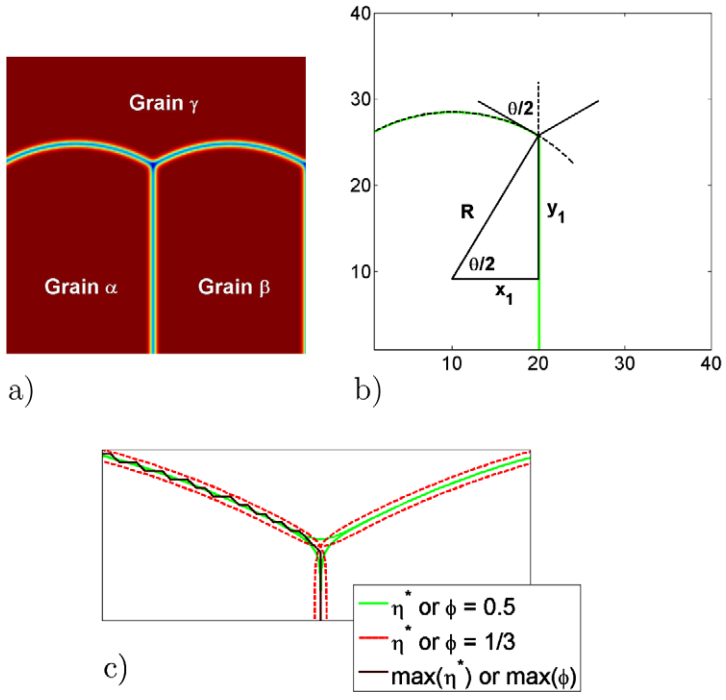

Fig. 2. (a) Diffuse interface representation of the studied three-grain structure during steady-state grain boundary motion. (b) Construction used to determine the triple junction angle. R is the radius of a circle fitted through the contour $\eta^*_\alpha = 0.5$ or $\phi_\alpha = 0.5$. The triple junction angle θ can be calculated from $\theta = 2\arccos(x_1/R)$ with x_1 half the width of a lamella. (c) Contour lines for η^* or ϕ equal to 0.5 and 0.33 near the triple junction and the separation line for grain α in a sharp interface representation obtained by dividing the system into different regions depending on which phase field has the highest value.

$$R = \frac{x_1}{\cos\left(\frac{\theta}{2}\right)} \qquad \Rightarrow \qquad \theta = 2\arccos\left(\frac{R}{x_1}\right), \tag{33}$$

with θ, R and x_1 as indicated in Fig. 2b. As illustrated in Fig. 2c, the curvature of the contour lines for constant value of ϕ_α or η^*_α deviates from that of the grain boundary near the triple junction. Therefore, points within a distance of approximately $1.5\,\varepsilon$ from the triple junction were omitted for the fitting. Although the results are somewhat sensitive to the number of grid points actually used in the fit and to the contour line for which the fit is made, this technique gives a fairly good indication of how well the expected triple junction angles are reproduced in the simulations. Beside this, we also determined the shrinkage rate of the grains α and β, which is an indirect measure of how well the triple junction angle is reproduced. It namely follows from relations (31) and (32), that a deviation of the triple junction angle results in a change of the shrinkage rate. Since the contour lines deviate from the actual grain boundary curve near the triple junction, it is also not possible to calculate accurately the angles between the boundaries at triple junctions directly from the values of the phase fields and their gradients.

Values for the triple junction angle θ and shrinkage rate dA_α/dt, obtained for different ratios of the specific grain boundary energies $\sigma_{\alpha\beta}/\sigma_{\alpha\gamma}$, for different grid spacings and interfacial widths ε, are compared with the theoretically expected values for both models in Table 3. The data were measured when grain boundary movement was steady-state (for some configurations it requires long time and a large system to reach steady-state).

For the considered grid spacings and interface widths, the triple junction angles and shrinkage rate obtained in the simulations are mostly close to the theoretical values, except for θ around 90°. As for the circular grain, the accuracy mainly depends on the ratio $\varepsilon/\Delta x$. Differences between the data obtained for both models are of the same order as the errors on the data. There is no clear systematic deviation between the data obtained for both models. For both models, a much finer grid spacing is required to reproduce the small triple junction angles ($\theta \leqslant 90°$) well. For these angles, the results are more sensitive to the details of the measuring technique and may differ slightly when evaluated at different time steps. These difficulties with representing and measuring small angles are probably inherent to the discretized representation. Simulations for a system size twice as large give nearly the same values for the triple angles and shrinkage rates, which indicates that the lower accuracy for small triple junction angles is probably not introduced by the diffuse character of the boundaries.

In Fig. 3, the profiles of the phase fields across the grain boundaries between grains α and β and between grains α and γ (their spacial resolution along a line perpendicular to the boundary) are compared. The slopes of the profiles at the middle of the interfaces are equal for both models, but the shape of the profiles shows some differences. For the MPF model, the profiles are symmetrical and the phase fields always equal 0.5 at the middle of the interface. In the CF model, the value at which η_α and η_β intersect depends on the coefficient $\gamma_{\alpha\beta}$′ and differs for boundaries with a different energy (compare plot (a) and (b)). The multi-obstacle potential in the free energy of the MPF model (2) also results in an interface region that is defined more strictly, whereas the free energy in the CF model leads to more diffuse profiles.

5. Multi-grain structures

Except from the fact that the phase-field profiles at the interface have a different shape, the two models do not show significant differences in grain boundary migration for the test configurations considered in the previous section. In this section, both models are applied to normal and textured grain growth in limited 2D and 3D grain assemblies. Three cases will be considered, namely normal grain growth in 2D with $\sigma = 0.25$ and $\mu = 1$ for all grain boundaries, normal grain growth in 3D with $\sigma = 0.25$ and $\mu = 1$ and grain growth in a 2D systems with two texture components and accordingly two types of boundaries. For the latter case, the grain structure is assumed to consist of two types of grains, A and B, as shown in Fig. 4b. Grain boundaries between grains of the same type have a grain boundary energy $\sigma_{AA} = \sigma_{BB} = 0.20$ and those between grains of a different type have $\sigma_{AB} = 0.25$. The grain boundary mobility of all grain boundaries equals $\mu = 1$.

The initial structures were obtained by dividing domains of 502×502 (2D) or $202 \times 202 \times 202$ (3D) grid points into 75 grains according to a Voronoi diagram based on a random set of 75 points and assuming periodic boundary conditions. For the 2D simulations, the Voronoi structure evolved for 6000 time steps using the simulation parameters given below and $\sigma = 0.25$ and $\mu = 1$ for all boundaries. The resulting structure, an ensemble of 71 grains with triple junction angles of 120°, was then used as the start configuration for continuing the 2D simulations. The 3D sim-

Table 3
Equilibrium angle at the triple junction and temporal evolution of the area of grain α for the MPF and CF model are compared with the analytical value for different grain boundary energy ratios $\sigma_{\alpha\beta}/\sigma_{\alpha\gamma}$, different grid spacings Δx and different interface widths ε. $\gamma_{\alpha\beta\delta}$ in the MPF potential is 3.0 for all cases.

σ	Δx, ε	θ			dA_α/dt		
		Anal.	MPF	CF	Anal.	MPF	CF
$\sigma_{\alpha\beta} = \sigma_{\alpha\gamma} = \sigma_{\beta\gamma} = 0.25$	$\Delta x = 0.1$ $\varepsilon = 0.5$	120°	119°	119°	0.25	0.26 (2.8%)	0.26 (4.0%)
$\sigma_{\alpha\beta} = \sigma_{\alpha\gamma} = \sigma_{\beta\gamma} = 0.25$	$\Delta x = 0.2$ $\varepsilon = 1.0$	120°	119°	118°	0.25	0.26 (2.8%)	0.26 (4.3%)
$\sigma_{\alpha\beta} = 0.25$, $\sigma_{\alpha\gamma} = \sigma_{\beta\gamma} = 0.2$	$\Delta x = 0.1$ $\varepsilon = 0.5$	103°	100°	105°	0.25	0.26 (6.0%)	0.25 (1,1%)
$\sigma_{\alpha\beta} = 0.25$, $\sigma_{\alpha\gamma} = \sigma_{\beta\gamma} = 0.2$	$\Delta x = 0.2$ $\varepsilon = 1.0$	103°	100°	104°	0.25	0.26 (6.0%)	0.25 (0.2%)
$\sigma_{\alpha\beta} = 0.2$, $\sigma_{\alpha\gamma} = \sigma_{\beta\gamma} = 0.25$	$\Delta x = 0.2$ $\varepsilon = 0.5$	133°	135	133°	0.20	0.19 (5.9%)	0.20 (0,1%)
$\sigma_{\alpha\beta} = 0.25$, $\sigma_{\alpha\gamma} = \sigma_{\beta\gamma} = 0.175$	$\Delta x = 0.2$ $\varepsilon = 1.0$	89°	84°	97°	0.25	0.27 (8.9%)	0.24 (4,7%)
$\sigma_{\alpha\beta} = 0.175$, $\sigma_{\alpha\gamma} = \sigma_{\beta\gamma} = 0.25$	$\Delta x = 0.2$ $\varepsilon = 1.0$	139°	139°	139°	0.175	0.174 (0.6%)	0.173 (0.8%)
$\sigma_{\alpha\beta} = 0.25$, $\sigma_{\alpha\gamma} = \sigma_{\beta\gamma} = 0.36$	$\Delta x = 0.2$ $\varepsilon = 1.0$	139°	139°	139°	0.25	0.25 (0.6%)	0.24 (0.8%)

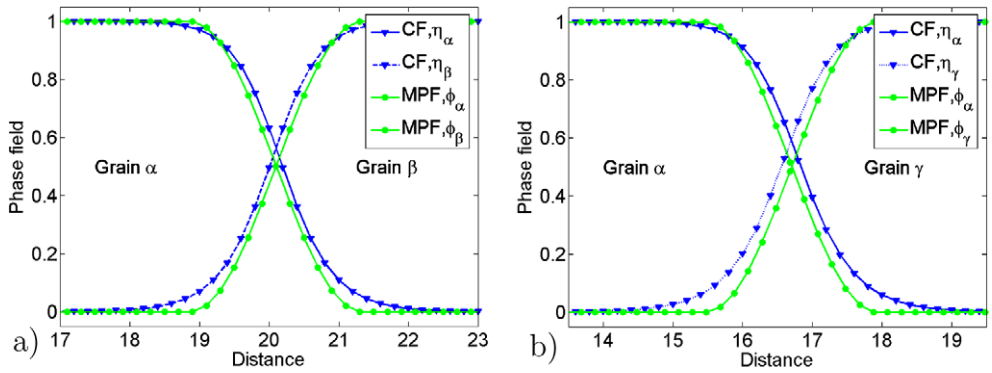

Fig. 3. Comparison of the phase-field profiles at the interfaces for the three-grain structure with $\sigma_{\alpha\beta} = 0.25$ and $\sigma_{\alpha\gamma} = \sigma_{\beta\gamma} = 0.2$ for steady-state grain boundary movement. (a) Profiles across the immobile interface between grains α and β. (b) Profiles across the moving interface between the grain α and γ. System parameters: $\mu = 1$, $\varepsilon = 1$, $\Delta x = 0.2$, $\ell_1 = \ell_2 = 40$.

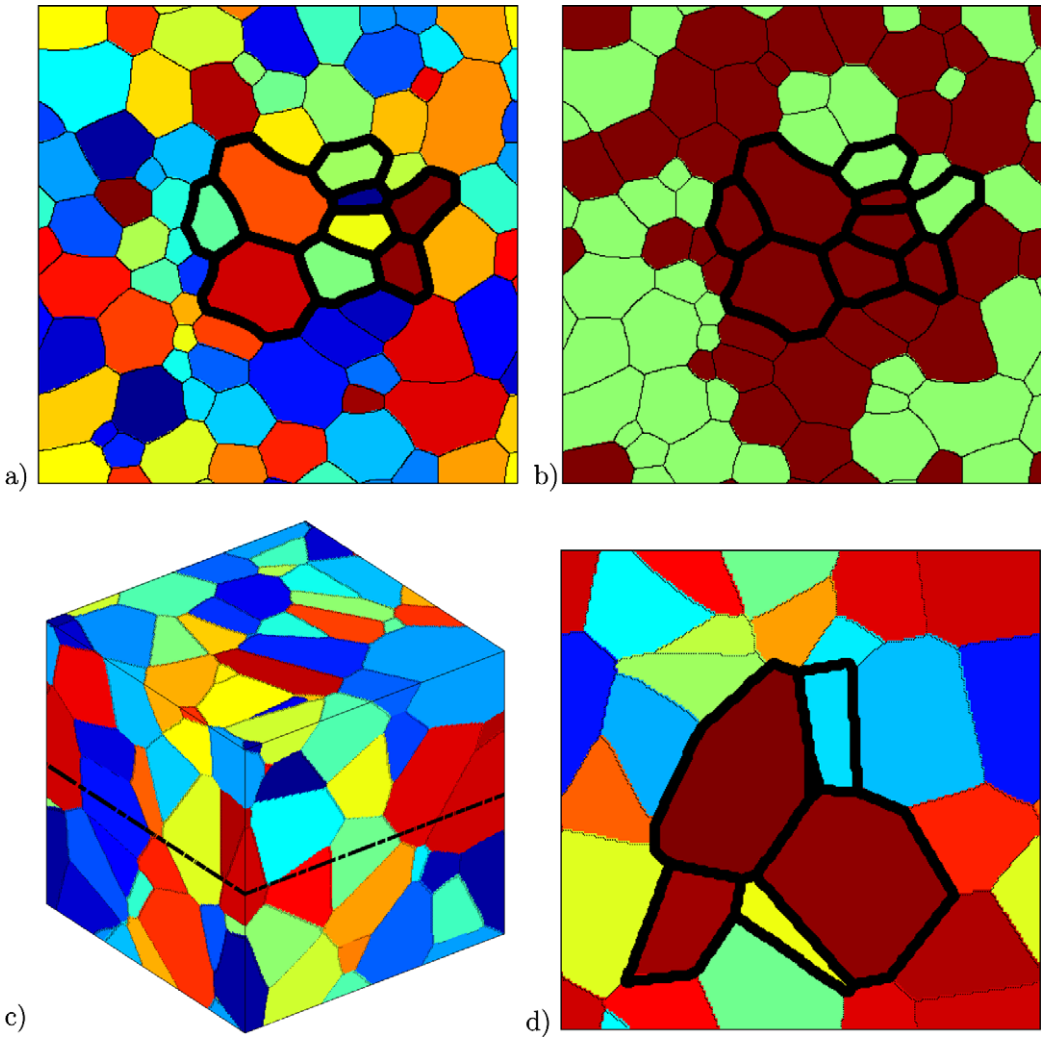

Fig. 4. Initial grain structures used in this study. (a) Normal grain growth in 2D. (b) Grain growth in a 2D structure with two types of grains, labeled A (light green) and B (dark red). (c) Normal grain growth in 3D. (d) 2D-section of the 3D structure in (c). The evolution of the grains indicated with a bold contour is compared in detail in the next section. (For interpretation of the references to color in this figure legend, the reader is referred to the web version of this article.)

ulations started from a 3D Voronoi structure with arbitrary triple-junction angles and flat grain boundaries. The initial structures for the three cases are shown in Fig. 4. A grid spacing of $\Delta x = 0.2$, time step $\Delta t = 0.03$ for 2D and $\Delta t = 0.015$ for 3D, and diffuse interface width of $\varepsilon = 1$ were used, giving a total system size of $\ell_1 = \ell_2 = 100.4$ for the 2D systems and $\ell_1 = \ell_2 = \ell_3 = 40.4$ for the 3D system. The coefficients $\gamma_{\alpha\beta\delta}$ in the MPF potential were equal to 3.0 for the 2D systems and 2.25 for the 3D system. From the results in Section 4.2, we expect that a ratio $\varepsilon/\Delta x = 5$ gives reasonably accurate simulation results for both models. For all

simulations, the contours $\phi = 0.5$ or $\eta^* = 0.5$, the size and number of neighbors were determined for all grains at every 1000 time steps. First, the evolution of individual grains in these multi-grain structures is compared for both models. Then, the statistics of the grain structures are compared with mean field theories and those obtained from previous simulations for grain growth. The number of grains considered in the simulations is too small to obtain reliable grain growth statistics. The goal is however to compare the behavior of the individual grains and to study to which extend deviations affect the evolution of the surrounding grain structure.

5.1. Evolution of individual grains

In the Figs. 5 and 6, the evolution of the selected grains in the CF and MPF simulations is compared in detail for the 2D structure with *A* and *B* grains and the 3D structures with equal grain boundary energies by plotting the contour $\phi = 0.5$ or $\eta^* = 0.5$ for each grain. The overall evolution of the grain assembly is the same for both models. Near disappearing grains, larger deviations between the position of the grain boundaries occur locally and for a short time period in both simulations. Disappearing grains have the tendency to shrink faster in the CF simulations than in the MPF simulations. Once a grain has disappeared, the contours match well again. The first pictures in Fig. 6 show that it takes more time in the MPF-simulation for the structure to evolve from the initial Voronoi configuration with highly non-equilibrium triple-junction angles and straight grain boundaries towards a typical grain configuration. The evolution temporarily follows a slightly different path. After some time the contour plots match, except around disappearing grains. This difference must be due to the different form of the free energy used in both models and not due to a different mobility or drag effect of the triple junctions. Once the triple junctions have a configuration close to that required for thermodynamic equilibrium and the boundaries have obtained their curvature, the triple junctions no longer affect the grain growth kinetics. For none of the models, the triple junctions drag the boundaries when they are close to equilibrium.

In Fig. 7, the volume and number of faces as a function of time is plotted for a longer time period for the selected grains in the 3D case. Although the evolution of the volumes of the grains is not exactly the same in both simulations and the grains do not undergo exactly the same neighbor switching events, the curves for one grain do not diverge. When the behavior deviates at a certain point, it recovers again after some time. The attraction towards a particular growth regime with, for example steady-state grain growth characteristics, seems to be so strong that deviations in the behavior of individual grains cannot amplify or disturb the overall growth behavior. This observation can be generalized to other mesoscale simulation techniques of grain boundary motion as well as to grain growth in real systems.

The curves in Fig. 7 illustrate that the evolution in the MPF-simulations is slower. A combined consideration of the images and the contour plots in Fig. 6 reveals that in fact only the smallest grains evolve faster in the CF simulations, while the contour lines for boundaries far from a disappearing grain for both models match well. The faster disappearance of the smallest grains in the CF simulations induces an earlier transition in the number of faces and growth behavior of the grains in its environment.

There are several reasons for the small variations between the simulation results obtained with both phase-field approaches. An important factor is the use of a different free energy potential. As illustrated in Fig. 3, the double-obstacle potential in the MPF free energy results in transitions of the phase fields within a well-defined interfacial region whereas the free energy in the CF model causes transitions with a longer tail. For both models, the width of the interfaces is taken wider than the physical grain boundary width and the grain boundary profiles therefore interact over a large distance. Due to the longer tails, the phase-field profiles in the CF simulations interact over a greater distance than in the MPF simulations. Furthermore, an algorithm using a locally reduced number of phase fields, similar to the procedure given in [12], was used for the MPF simulations for multi-grain structures. This algorithm calculates only the values of a limited number of phase fields, namely those with the highest values, at each grid point, whereas the full set of equations is solved for all phase fields in the CF simulations. It was shown in [12] that a reduction in the number of phase fields considered at each grid point may retard the disappearance of small grains. The differences result in a faster shrinkage rate for small grains in the CF simulations and a slower adaptation of triple junctions far out of equilibrium in the MPF. If desirable, the shrinkage rate of small grains in the CF model can be reduced by using a smaller interface width. This requires a smaller grid spacing to maintain numerical stability and accuracy. The reaction of triple junctions in the MPF model can be enhanced either by using a larger interface width, by a smaller grid spacing or by considering more phase fields at each grid point in the sparse-data structure algorithm. It will be shown in the following subsection, however, that the detailed characteristics of individual grains on the local scale have almost no effect on the grain growth kinetics of the full system. This was also shown in the results from large-scale phase-field simulations [6,10–12].

5.2. Comparison with mean field theories and previous simulation results

In Fig. 8, the growth rate obtained for grains of different topological classes, i.e. with a defined number of sides (2D) or faces

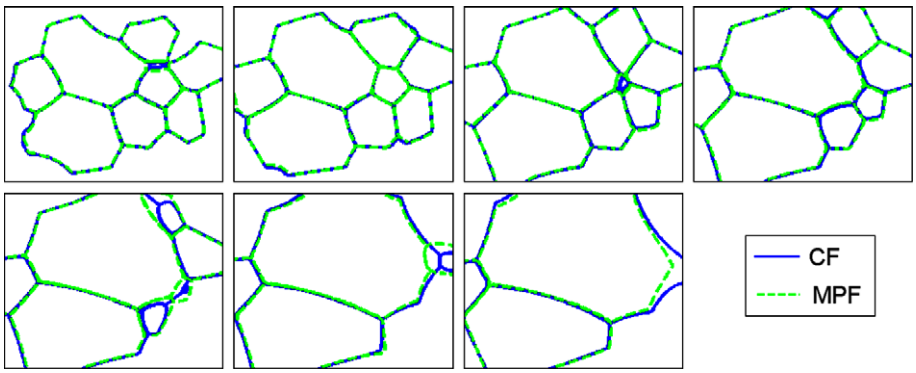

Fig. 5. Grain contours at $\phi = 0.5$ and $\eta^* = 0.5$ for different time steps of the selected grains in the 2D structures (indicated in bold in Fig. 4) obtained from MPF and CF simulations for the structure with two types of grains. Images from left to right are for times $t = 150, 300, 600$ and 900 (first row) and 1200, 1500 and 1800 (second row).

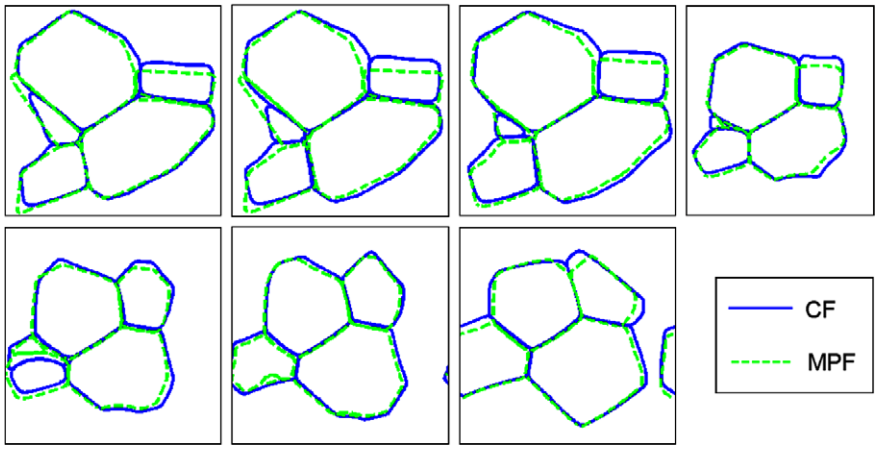

Fig. 6. Grain contours (at $\phi = 0.5$ and $\eta^* = 0.5$) for different time steps of the grains in the selected section of the 3D simulation with uniform grain boundary properties. Images from left to right are for times $t = 7.5, 15$, 30 and 90 (first row) and 150, 225 and 450 (second row).

(3D), are compared with analytical theories for normal grain growth, for 2D and 3D with equal grain boundary energies. The data were obtained for grains remaining in the same topological class for at least 5000 time steps of which the first and last 500 time steps are omitted. For the 3D application, the first 10,000 time steps, where the triple-junctions are not in equilibrium and grain boundaries do not have their expected curvature, are omitted as well.

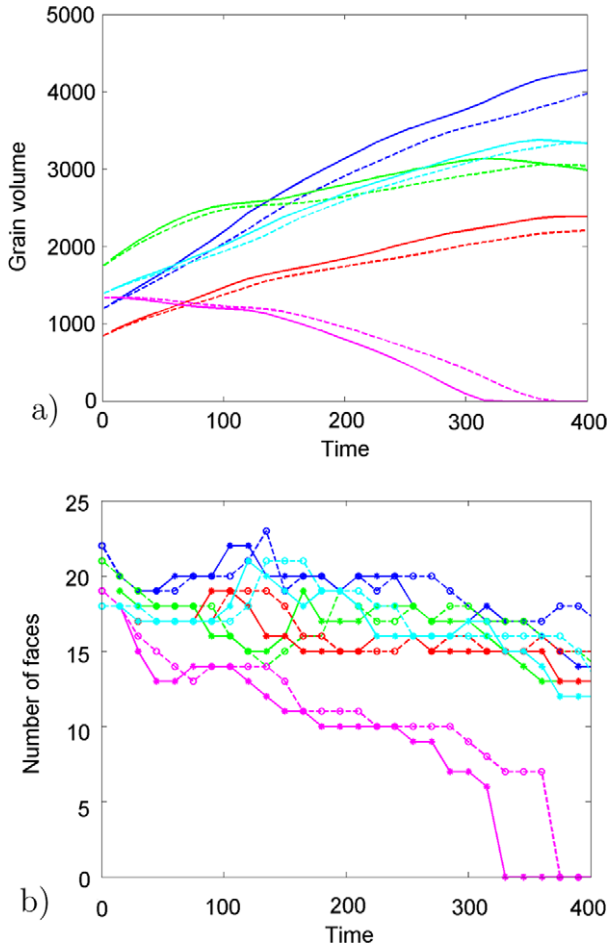

Fig. 7. Evolution of (a) the grain volume and (b) the number of sides for the selected grains in the 3D simulation for the CF (full line) and MPF (dashed line) model.

The von Neumann-Mullins relation for ideal grain growth in 2D states that the growth rate of a grain with n sides equals [19,20]

$$\frac{dA}{dt} = \frac{\pi}{3}\mu\sigma_{gb}(n-6) = k_{NM}(n-6). \tag{34}$$

This law is valid for any connected grain structure with equal grain boundary energies and, accordingly, angles of 120° at triple junctions, but does not require steady-state grain growth or a particular grain size distribution. It is thus valid for our simulation systems. The data points in Fig. 8a show that the von Neumann-Mullins relation is indeed very well reproduced by both models. Fitting a linear relation through the data points gives a slope equal to 0.266 for the CF simulations and 0.256 for the MPF simulations, whereas a slope equal to 0.262 is expected from relation (34). In accordance with the observations discussed in Section 5.1, growth ($n > 6$) and shrinkage ($n < 6$) are slightly faster in the CF than in the MPF simulations. The values of the slopes demonstrate that this effect is negligibly small, especially if one is interested in the average growth kinetics of a large grain structure.

In 3D, the growth rate of a grain does not solely depend on its number of faces, but also on its shape. Assuming all grain faces are pentagons, Mullins [21] derived an approximate relation for the average growth rate of grains with a given number of faces n_f:

$$\left\langle \frac{1}{R}\frac{dV}{dt} \right\rangle = M\sigma_{gb}F(n_f)G(n_f), \tag{35}$$

with

$$F(n_f) = \pi/3 - 2\arctan[1.86(n_f-1)^{1/2}/(n_f-2)], \tag{36}$$

and

$$G(n_f) = 5.35n_f^{2/3}\left(\frac{n_f-2}{2(n_f-1)^{1/2}} - 3/8F(n_f)\right)^{-1/3}. \tag{37}$$

A similar relation was obtained by Hilgenfeldt et al. [22] using different assumptions about the shape of the grains and faces. A simplification of the exact relation for the growth rate of individual grains in ideal 3D grain structures, derived by MacPherson and Srolovitz, leads to an equivalent dependence for the average growth rate on the number of faces [23]. This relation is derived assuming triple junction angles close to 120°, but does not assume steady-state grain growth, and should thus apply for the later time steps of the 3D simulations. Fig. 8b shows that our simulation data

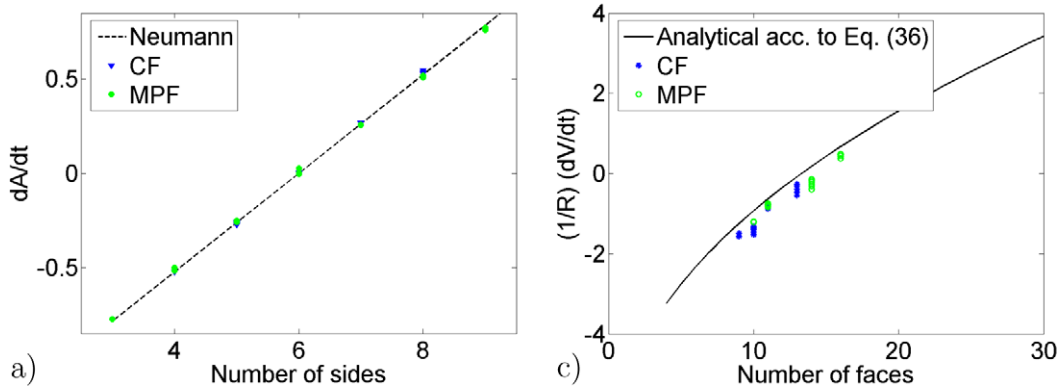

Fig. 8. Growth rates of grains of different topological classes determined at different time steps from the CF and MPF simulations for the (a) 2D and (b) 3D cases with equal grain boundary energies. The data points are compared with the von Neumann–Mullins relation (34) for 2D (dashed line) and with the approximate Mullins relation (35) for 3D (solid line).

are somewhat below the analytical curve (35), as is also the case for data obtained using a vertex model approach [24], from simulations with the Surface Evolver software [25] and on the basis of phase-field computations for larger systems [12]. There is no significant difference between the data points obtained from the CF and MPF simulations.

Although the number of grains in our simulations does not allow a derivation of statistical properties, the 2D and 3D simulations with equal grain boundary energies show a parabolic growth behavior over a certain time period. In Fig. 9a and b, the evolution of the average grain size as a function of time is plotted for time steps within this period. Curves obtained from mean field theories and from large-scale normal grain growth simulations are additionally considered for comparison. Mullins' law [26] predicts a parabolic growth rate according to

$$\overline{R}^2(t) = \overline{R}^2(0) + 2\beta\mu\sigma_{gb}\,t, \tag{38}$$

with $2\beta = 0.4$ for 2D systems and $2\beta = 0.5$ for 3D systems. The 2D phase-field simulations of Fan and Chen [6] were performed using a CF type of phase-field model. 3D phase-field simulations of normal grain growth have been performed by Krill and Chen [11] using a CF type of model, and by Kim and Kim [12] using a MPF type of model. For the 2D case, the growth rate obtained in the CF and MPF simulations is much lower than that predicted by Mullins [26] and that obtained with 2D vertex simulations [27]. Our data points obtained for both models are close to the curve obtained by Fan and Chen [6] for steady-state grain growth in larger grain structures. For 3D, there is better agreement on the value of β. Although the presented data points are very scattered due to the limited number of grains in the system, the overall growth behavior follows that predicted by large-scale simulations. The comparison of the data obtained from the considered phase-field approaches indicates that the growth behavior in ideal systems is unsensitive for small variations of the local behavior of individual grains. As long as there are enough grains in the system, local changes level out in time without affecting the overall growth kinetics.

In Fig. 10, results for grain growth in the system with *A* and *B* grains and two different grain boundary energies are shown. Both models give again very similar results, except that changes in the average properties of the system tend to be slightly earlier for the CF than for the MPF simulations. The contour plots in Fig. 5 show that there are in fact only differences around vanishing grains. We expect accordingly that the effect on the statistics of a grain structure is also negligible for systems with a large number of grains and over an extended period of grain growth. For both models, the initial growth rate for the two types of grains until $t = 500$ is almost the same as in the 2D simulation with equal grain boundaries. In this regime, grain growth is thus clearly governed by the high energy boundaries, or more specifically by the disappearance of grains with mainly high energy boundaries. The relative number of type B grains also increases considerably, because in the initial structure the grains of type A have on average boundaries with slightly higher energy than the type B grains. After the initial period, the average growth stagnates for some time; followed by a regime with again close to parabolic growth. The average grain size for both types of grains follows closely the overall

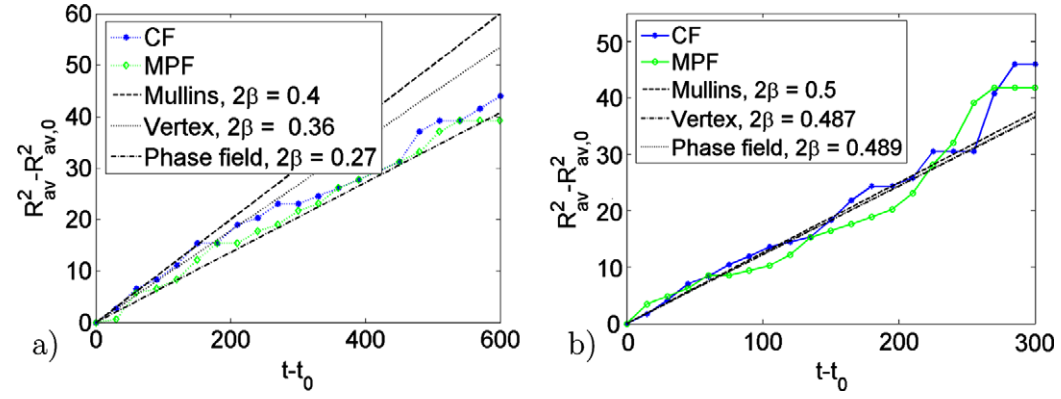

Fig. 9. Comparison of the evolution of the average grain size squared R^2_{av} in the (a) 2D and (b) 3D simulations with equal grain boundary energies for the PFM and CF model. The analytical relations $R^2_{av} - R^2_{av,0} = 2\beta\mu\sigma_{gb}t$ with $2\beta = 0.4$ for 2D and $\beta = 0.5$ for 3D from [26] are added for comparison. Relations obtained from simulations using vertex models (from [27] for 2D and from [24] for 3D) and using phase-field models (from [4] for 2D and from [12] for 3D) are also added.

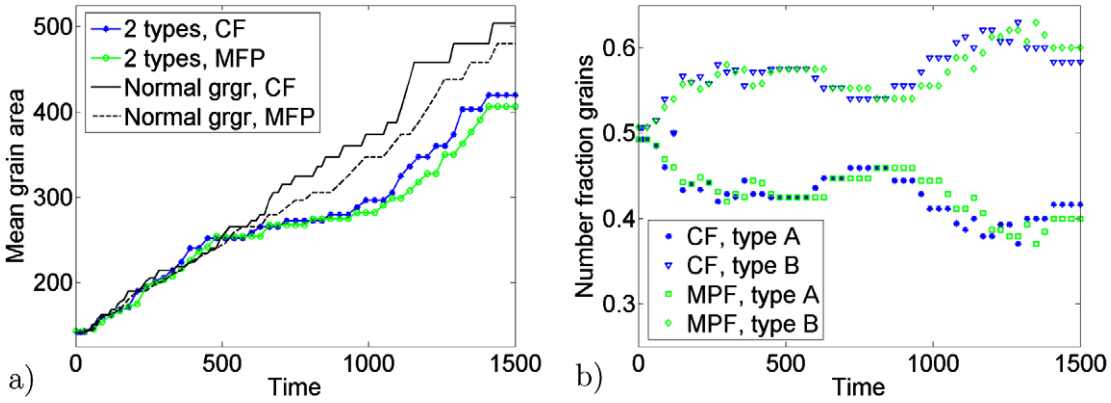

Fig. 10. Evolution of the (a) average mean grain size and (b) relative fraction of each type, as a function of time for the case with two types of grains for the CF and the MPF model. The evolution of the mean grain size is compared with that for the 2D case with equal grain boundaries (normal grain growth). The evolution of the average grain size of each type of grains follows approximately that of the overall mean grain size.

mean grain size. Although, the described step-wise growth with strengthening of the major texture component in the growth periods has been observed before for structures with two texture components in 2D [28–33] and 3D [34], it remains a challenge for further investigations whether this effect is recovered for large grain structures. It is clear that besides the fully steady-state grain growth observed for pure systems with equal grain boundary properties, this step-wise growth can accommodate as well for the small deviations in behavior of disappearing grains.

6. Conclusions

Different phase-field approaches have been proposed in literature to simulate grain growth on the mesoscale, using different model variables, model parameters and formulations of the thermodynamic free energy. Although the final evolution equations differ between different approaches, for many of them it has been shown that they are able to reproduce established mean field and statistical theories for normal grain growth in large grain structures. However, it was never verified rigorously whether the evolution of individual grains and grain boundaries is identical and how small local variations influence the overall grain growth kinetics.

We have compared in detail the model formulations and their application for two phase-field approaches of grain growth. Simulations were performed for simple two- and three-grain structures, for structures with a limited number of grains, and for different values of the grain boundary energies. The effect of the diffuse interface width and discrete grid spacing on the numerical results was studied as well. For equivalent model parameter combinations, the differences between the simulation results obtained with both models are smaller than effects from changing the grid spacing or interface width. Though, the shrinkage rate of small grains in the multi-grain structures is different for both models and accordingly around these small grains, there are locally large discrepancies in the grain structure. These deviations are of temporary kind and only affect the shape of the nearest neighboring grains. Once the small grain has vanished, the structures match well again after a short evolution time. If the simulation starts from a structure with triple junction angles far from those required for thermodynamic equilibrium, as for a grain structure generated according to a Voronoi diagram, there are temporarily large differences in the evolution of the grain structures. This is due to the different form of the free energy functional used in both approaches. The structures however match quickly once the triple junction angles are close to those required for thermodynamic equilibrium in both simulations.

In our simulations for multiple grain configurations, the systems were evolving towards a regime with steady-state grain growth characteristics and showed a step-wise growth changing between two characteristic growth regimes in the case of two different types of grain boundaries. The tendency to evolve towards such regimes is so strong that small fluctuations in the shape of individual grains are annihilated after a limited time of grain growth and hardly affect the overall properties of grain growth. This last conclusion is generally true for other mesoscale simulation techniques of grain growth, and seems to reflect a natural organizing principle. If the grain structure contains impurities or if the grain orientation, grain size distributions or grain boundary characteristics are very inhomogeneous, there might not be such a regime of attraction towards which the system is redirected when the behavior of an individual grain deviates. A better understanding of the atomic mechanisms by which grains disappear and triple junctions rearrange is required to validate the models more quantitatively with respect to such phenomena.

We conclude that generally grain growth in bulk materials is mainly determined by the energies and mobilities of the grain boundaries. In most applications, the overall growth behavior is not affected by small deviations in the behavior of individual grains or grain boundaries. Both phase-field approaches are therefore suitable to study the statistics and mean field characteristics of grain growth in bulk materials, even if they do not result in identical dynamics for vanishing grains.

Acknowledgement

NM is postdoctoral fellow of the Research Foundation – Flanders (FWO-Vlaanderen). FW and BN acknowledge the financial support of the German Federal Ministry of Education and Research (BMBF) under Grant No. FKZ 1708X06.

References

[1] W. Boettinger, J. Warren, C. Beckermann, A. Karma, Annu. Rev. Mater. Res. 32 (2002) 163–194 (review article).
[2] L.-Q. Chen, Annu. Rev. Mater. Res. 32 (2002) 113–140.
[3] I. Singer-Loginova, H.M. Singer, Rep. Prog. Phys. 71 (2008) 106501:1–106501:32.
[4] N. Moelans, B. Blanpain, P. Wollants, Calphad 32 (2008) 268–294.
[5] L.-Q. Chen, W. Yang, Phys. Rev. B 50 (1994) 15752.
[6] D. Fan, L.-Q. Chen, Acta Mater. 45 (1997) 611–622.
[7] I. Steinbach, F. Pezzolla, B. Nestler, M. Seeßelber, R. Prieler, G.J. Schmitz, J.L.L. Rezende, Physica D 94 (1996) 135–147.
[8] H. Garcke, B. Nestler, B. Stoth, SIAM J. Appl. Math. 60 (1999) 295–315.
[9] N. Moelans, B. Blanpain, P. Wollants, Phys. Rev. B 78 (2008) 024113.
[10] D. Fan, C. Geng, L.-Q. Chen, Acta Mater. 45 (3) (1997) 1115–1126.
[11] C. Krill III, L.-Q. Chen, Acta Mater. 50 (2002) 3057–3073.

[12] S. Kim, D. Kim, W. Kim, Y. Park, Phys. Rev. E 74 (2006) 061605.
[13] B. Nestler, H. Garcke, B. Stinner, Phys. Rev. E 71 (2005) 041609.
[14] N. Moelans, B. Blanpain, P. Wollants, Phys. Rev. Lett. 101 (2008) 025502.
[15] R. Kobayashi, J.A. Warren, W.C. Carter, Physica D 119 (1998) 415–423.
[16] T. Pusztai, G. Bortel, L. Granasy, Europhys. Lett. 71 (2005) 131–137.
[17] H. Garcke, B. Nestler, B. Stinner, SIAM J. Appl. Math. 64 (2004) 775–799.
[18] A. Kazaryan, Y. Wang, S. Dregia, B. Patton, Phys. Rev. B 63 (18) (2001) 184102.
[19] J. von Neumann, Metal Interfaces, American Society of Testing Materials, Cleveland, 1952. pp. 108–110.
[20] W. Mullins, J. Appl. Phys. 27 (8) (1956) 900–904.
[21] W. Mullins, Acta Metall. 37 (1989) 2979–2984.
[22] S. Hilgenfeldt, A. Kraynik, S. Koehler, H. Stone, Phys. Rev. Lett. 86 (2001) 2685–2688.
[23] R. MacPherson, D. Srolovitz, Nature 446 (2007) 1053–1055.
[24] D. Weygand, Y. Bréchet, Philos. Mag. B 79 (1999) 703–716.
[25] F. Wakai, N. Enomoto, H. Ogawa, Acta Mater. 48 (2000) 1297–1311.
[26] W. Mullins, Acta Mater. 46 (1998) 6219–6226.
[27] D. Weygand, Y. Bréchet, J. Lépinoux, Philos. Mag. B 78 (1998) 329–352.
[28] K. Mehnert, P. Klimanek, Scripta Mater. 30 (1996) 699–704.
[29] K. Mehnert, P. Klimanek, Comput. Mater. Sci. 9 (1997) 261–266.
[30] H. Eichelkraut, G. Abbruzzese, K. Lucke, Acta Metall. 36 (1988) 55–68.
[31] Y. Novikov, Acta Metall. 27 (1979) 1461–1466.
[32] N. Hwang, B.-J. Lee, C. Han, Scripta Mater. 37 (11) (1997) 1761–1767.
[33] N. Ma, A. Kazaryan, S. Dregia, Y. Wang, Acta Mater. 52 (13) (2004) 3869–3879.
[34] O. Avasishin, S. Shevchenko, N. Vasiliev, S. Semiatin, Acta Mater. 51 (2003) 1019–1034.